Electrical Power and Energy Systems 115 (2020) 105452

Contents lists available at ScienceDirect

Electrical Power and Energy Systems

journal homepage: www.elsevier.com/locate/ijepes

A selective harmonic compensation and power control approach exploiting distributed electronic converters in microgrids

Augusto Matheus dos Santos Alonso[a,b,*], Danilo Iglesias Brandao[c], Tommaso Caldognetto[d], Fernando Pinhabel Marafão[a], Paolo Mattavelli[d]

[a] Group of Automation and Integrated Systems, Sao Paulo State University (UNESP), Av. Três de Março 511, 18087-180 Sorocaba, Sao Paulo, Brazil
[b] Department of Electric Power Engineering, Norwegian University of Science & Technology (NTNU), O.S. Bragstads plass 2, 7491 Trondheim, Norway
[c] Graduate Program in Electrical Engineering, Federal University of Minas Gerais (UFMG), Av. Antônio Carlos 6627, 31270-901 Belo Horizonte, Minas Gerais, Brazil
[d] Department of Management and Engineering, University of Padova, Stradella San Nicola 3, 36100, Vicenza, Italy

ARTICLE INFO

Keywords:
Distributed converters
Harmonic compensation
Hierarchical control
Power quality
Power sharing

ABSTRACT

This paper proposes an approach to obtain harmonic compensation and power control by exploiting the electronic power converters deployed in low-voltage microgrids. By the proposed approach, distributed harmonic current compensation is achieved without interfering with the converter's power exchange involved in interfacing the local energy resources (e.g., renewable sources, storage devices) with the grid. The control framework refers to a master/slave microgrid architecture where distributed power converters play as slave units, coordinated by a centralized controller; the data exchange among agents occurs periodically, concerns current magnitudes only, and can be fulfilled by communication means of limited performance. The paper shows the achievable results in terms of power quality improvements and discusses the challenges related with the aimed objective. The proposed methodology is evaluated by means of simulation and experimental tests on a single-phase low-voltage microgrid prototype comprising nonlinear loads and two converters. Different cases of generation limits, load variations, voltage levels, voltage distortions, and line parameters are considered in the tests reported. In addition, the robustness of the proposed method to non-ideal and faulty communication links is discussed and shown by means of experimental results.

1. Introduction

Nonlinear loads connected to electrical grids introduce voltage and current distortions that affect the regular system operation (with, e.g., capacitors resonances, false trips of circuit [1]) and may be found exacerbated in specific scenarios like the one of low-voltage (LV) microgrids [2,3]. To reduce harmonics and reactive current circulation and comply with electrical codes, passive and active filters have been extensively used over the years [4,5].

Nowadays, with the recent decentralization trends in power systems and the actual implementation of microgrids (MGs), the multifunctional switching power interfaces (SPIs) employed to interface energy resources with the LV network are going to play a crucial role in ensuring and, possibly, improving the quality of supply [6,7]. This is possible by exploiting the SPIs power capabilities left available after having fulfilled their major purpose of injecting active power. From this perspective, this paper (*i*) presents a technique to use distributed SPIs in order to achieve distributed harmonic compensation without interfering with their main purpose of delivering active and reactive power and (*ii*) shows the results that can be achieved by using distributed SPIs to provide harmonic compensation, reporting the possible power quality improvements and discussing the issues related with the matter.

In microgrids, hierarchical control approaches shown to be effective in providing active and reactive power control and integrating these fundamental functionalities with more advanced ones like distributed harmonic compensation [8–11]. Droop control is frequently adopted in such control structures [11–15]. The main challenge of droop-based solutions is balancing the trade-off between power-sharing accuracy and grid-voltage amplitude and frequency regulation, as well as damping the oscillations of the power exchanged among sources [16]. To cope with these aspects, in [17] extra droop loops are used for harmonic voltage reduction and harmonic sharing, whereas in [18] a model predictive control approach is applied to compensate voltage unbalances and limit overcurrents. In [19] a virtual admittance loop

---

[*] Corresponding author at: Department of Electric Power Engineering, Norwegian University of Science & Technology (NTNU), O.S. Bragstads plass 2, 7491 Trondheim, Norway.

E-mail address: augusto.alonso@ntnu.no (A.M. dos Santos Alonso).

https://doi.org/10.1016/j.ijepes.2019.105452
Received 17 January 2019; Received in revised form 15 June 2019; Accepted 29 July 2019

Nomenclature

Acronyms

CBC	Current-Based Control
DSO	Distribution System Operator
MG	Microgrid
SPI	Switching Power Interface

Marks

$\|\|$	In-phase component
$\perp$	Quadrature component

Variables

i_{local}	Local current of a node
i^{n*}	Time-domain current reference of the n-th SPI
I_h^*	Reference peak current for the N SPIs at the MG
I_h^{fn}	Peak current of the n-th SPI at harmonic h
I_{max}^{fn}	Maximum peak value of active current of the n-th SPI
I_{nom}^{fn}	Nominal peak current of the n-th SPI
I_h^{ft}	Total peak current of the N SPIs at the MG
I_{max}^{ft}	Total maximum peak value of active current of N SPIs at the MG
I_{nom}^{ft}	Total nominal peak current of the N SPIs at the MG
I_h^G	Grid peak current at harmonic h
I_h^{G*}	Reference for the grid peak current at harmonic h
I_h^L	Load peak current at harmonic h
ΔI	Availability of peak current considering N SPIs at the MG
ΔI^n	Availability of peak current of the n-th SPI
k	Actual cycle of the CBC control window
v_{local}	Local voltage of a node
x_h	Unitary sinusoidal reference of harmonic h
α_h^*	Scaling coefficient broadcasted for the N SPIs
θ_h	Phase angle of the harmonic h
θ_n	Phase shift of node n's voltage in relation to PCC voltage
ω	Fundamental angular frequency

and a virtual capacitive impedance loop are included to obtain current or voltage harmonic attenuation during grid-connected or islanded operation, respectively. All these methods require previous knowledge about line impedances or network topology, requirements that are overcome in the approach presented herein.

For what specifically concerns harmonic compensation in hierarchically controlled systems, the authors in [20] propose a two-layer hierarchical control for coordination of SPIs, which is based on a selective resistive/inductive virtual impedance loop at the primary level and a technique for voltage harmonic distortion compensation at the secondary level; in such a proposal, SPIs overloading is not directly managed and voltage harmonic compensation requires dedicated devices like distributed shunt active power filters (APFs). In [21] a decentralized adaptive control method for reactive, harmonic, and unbalance power sharing, based on a consensus protocol, is discussed. Another study based on a consensus approach is presented in [22], using multi-objective scheduling optimization to enhance the MG's active and reactive power flow. Besides being implemented through droop control principles, [21,22] do not rely on the existence of a central controller and require communication among adjacent agents. The work described in [23] combines the concepts of variable virtual impedance and feedforward control to achieve uniform harmonic sharing without requiring communication, although power flow control at PCC is not considered. This latter concept presents an interesting way of exploiting SPIs capabilities without exceeding their nominal currents: the current harmonic sharing is achieved by a droop-related compensation factor that depends on the harmonic power availability of each SPI. On the other hand, based on an open-loop approach, the regulation and power sharing accuracies are directly affected by variations and non-idealities of system parameters. Another droop-based hierarchical approach, which is formulated with a secondary layer relying on a communication link, is presented in [9] to provide active and reactive power sharing. However, it does not allow distributed harmonic compensation among SPIs, neither controls power flow at the MG's PCC. Finally, [24] introduces a two-layer hierarchical strategy based on circulating currents. The primary layer comprises error compensation loops to cope with initially unknown network parameters, and based on a low-bandwidth communication link, a secondary controller drives voltage source SPIs toward the proportional sharing of reactive power and harmonic currents, similarly to [15]. The balancing of SPIs current contributions is obtained through a mixed scheme of synchronous (dq) and stationary ($\alpha\beta$) frame controllers. Besides, the defined distribution factors that proportionally coordinate SPIs are attained by power terms. Yet, since the authors devised the method for islanded mode, the control of active, reactive, and harmonic power flow at the PCC during grid-connected operation is instead not aimed or considered in [24], and SPIs are also susceptible to transient overcurrent stress due to the used virtual resistance, which requires adaptations as explained in [15]. Virtual resistance control is also adopted in [25] to formulate current sharing based on harmonic orthogonal components, as well as decomposition of currents at different sequences and orders through multi-second-order generalized integrators from frequency-locked-loops. Nonetheless, [25] presents similar limitations to [24] on the precise adoption of proportional resistance ratios to adequately share load currents among SPIs.

All this considered, despite the copious literature on this complex topic [11,14,15,17,19,23–25], distributed harmonic compensation by multifunctional SPIs in AC MGs is still an open and intriguing research topic.

1.1. Objectives and contributions

This paper proposes a harmonic compensation technique integrated in a hierarchical control framework for active and reactive power control implemented by means of a current-based control (CBC) approach. Its operation is also reported experimentally. The approach shows the following merits:

- The CBC achieves effective and accurate active, reactive, and harmonic current sharing among SPIs under generic voltage conditions in low-voltage microgrids;
- The algorithm provides fully-controllable power flow, high power factor, and low current distortion at the point of connection of the MG with the upstream grid;
- The centralized control strategy uses the information of current magnitudes collected from the distributed units at the central controller (CC) via a low-bandwidth communication link. The exchanged information does not require tight synchronization among nodes or knowledge of grid parameters, ensuring a practical implementation;
- Harmonics can be selectively mitigated with distributed SPIs while respecting their current capabilities.

The proposed controller is introduced in the following by referring to single-phase networks, nevertheless, it may be straightforwardly applied to three-phase systems too.

2. Microgrid control architecture and basics of harmonic selectivity

2.1. Network structure

Let us refer to the MG scenario depicted in Fig. 1, with linear and non-linear loads connected. It is composed of (*i*) a central controller, on which the secondary level is implemented at the MG's PCC; (*ii*) distributed slave units, incorporating energy resources (e.g., storage systems, renewables) and their multifunctional SPIs, called, together, energy gateways (EGs) [26]; (*iii*) a grid-forming converter connected at the PCC [3]; and (*iv*) a means of communication among EGs and the CC available for control purposes.

In such a structure, the grid voltage amplitude and grid frequency are defined by the main grid, under grid-connected operation, or by the grid-forming converter, during islanded operation [27,28]. In both modes of operation, the distributed units pursue the same global goal of sharing the MG current needs proportionally to their actual capabilities.

Typically, commercial grid-tied inverters behave as current sources [3,14] to more effectively comply with grid connection standards; this paper aligns with this situation and assumes that the SPIs are controlled as current sources (i.e., current-controlled converters). In general, dispatchable units operating as voltage sources (i.e., voltage-controlled converters) might also be considered in the supervised distribution network and integrated to the CBC; in this case, voltage-controlled converters should adjust their generated output voltage in order to follow the provided current reference given at their third control level [29,30].

It is worth remarking that the electrical network scenario considered herein is the one of low-voltage MGs, which refers to local power systems *i*) presenting clearly defined boundaries [31], *ii*) interconnecting sources and loads at the distribution voltage level [31,32], and *iii*) featuring advanced automation infrastructures and distributed generation units with limited power [32,33]. A reference model of the adopted application scenario may be considered the LV benchmark network proposed by CIGRE [32], in which the maximum length distance between a node of the network and the point of connection with the upstream grid is about 350 m. While of the scope of this work, further investigations may be performed to applications in different kinds of networks.

2.2. Hierarchical control structure and current-based control

The principle of operation of the CBC algorithm lies on the analysis, by the CC, of the current terms flowing through the PCC, so that control commands can be derived and dispatched to the EGs to perform the distributed compensation.

Considering the local operation of EGs, they implement the primary level of control, performing basic functions such as current/voltage control, synchronization, maximum power extraction, frequency/voltage regulation, islanding detection. Those local functions can be efficiently performed regardless of the status of other grid nodes [7] and may not rely on communication. Accordingly, under communication failures, the system may keep an efficient local operation, losing only those features that involve the exchange of information. Note that the proposed multi-loop scheme within [7] (i.e., comprising voltage support and DC link control loops, plus DC and AC output current control loops) is referred herein as primary controller, being responsible for controlling the converter's interaction with the grid, as seen in Fig. 1. Besides, any other desired additional features existing for grid-feeding inverters [3] (e.g., anti-islanding) could also be implemented without affecting the operational performance of the proposed coordinated control strategy.

The conventional secondary level of hierarchical control usually compensates amplitude and frequency deviations caused by the primary control [34]. In addition, secondary level may include other coordinated functions to improve the network operation, such as, voltage stabilization [9], reduction of distribution and conversion losses, effective load power sharing and disturbances compensation. Herein, the focus is on the accurate active, reactive, and harmonic current sharing among EGs. Thus, assuming that the steady-state operation of the system can be modified by adjusting the set-points of the local controllers, the CC processes the data collected over the grid and broadcasts references to the EGs by using the CBC algorithm.

The tertiary control is committed to manage the interaction between the network and the utility [5,34]. Within the considered hierarchical structure, the short-term energy management (i.e., power sharing) takes place at the secondary level, and the long-term energy management (i.e., grid current reference – I_h^{G*}), which may be defined with the distribution system operator (DSO), is managed at the tertiary level, as shown in Fig. 1.

The proposed selective harmonic compensation is located at the secondary level of control. It is described in the following.

2.3. Selective harmonic compensation principle

Selective harmonic compensation aims at fully or partially reducing specific harmonic components [35]. Using the CBC approach, the most harmful harmonics can be compensated by exploiting the available power capacity of the SPIs. Harmonic components identification is typically based on the discrete Fourier transform (DFT), which is here implemented by a time-domain approach that uses a phase-locked loop (PLL) and moving average filters (MAF).

As shown in Fig. 2(a), the PLL tracks the phase angle of the fundamental voltage (θ_1), which allows to calculate the terms $\theta_h = h{\cdot}\theta_1$, with "$h$" representing the harmonic order. These phases are fed to trigonometric functions to generate unitary reference signals that are in-phase ($x_{h\parallel}$) or quadrature ($x_{h\perp}$) to the measured nodal voltage (v_{local}). The adopted PLL structure is described in [36], where the selective signal generator is evaluated, showing its capability of ensuring immunity against voltage distortions and fundamental frequency deviations.

Fig. 2(b) shows how $x_{h\parallel}$ and $x_{h\perp}$ can be used to detect harmonic components from the nodal current (i_{local}). The algorithm obtains the peak values (amplitude) of the in-phase ($I_{h\parallel}$) and quadrature ($I_{h\perp}$) current terms for any targeted order h. It is highlighted that $I_{h\parallel}$ and $I_{h\perp}$ are average values, which can assume positive or negative values depending on how $x_{h\parallel}$ and $x_{h\perp}$ interact with the measured current i_{local}.

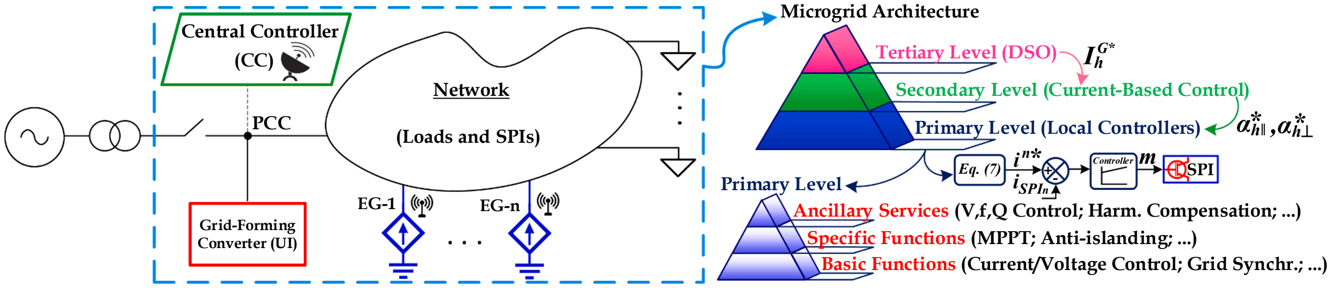

Fig. 1. Considered microgrid hierarchical control structure.

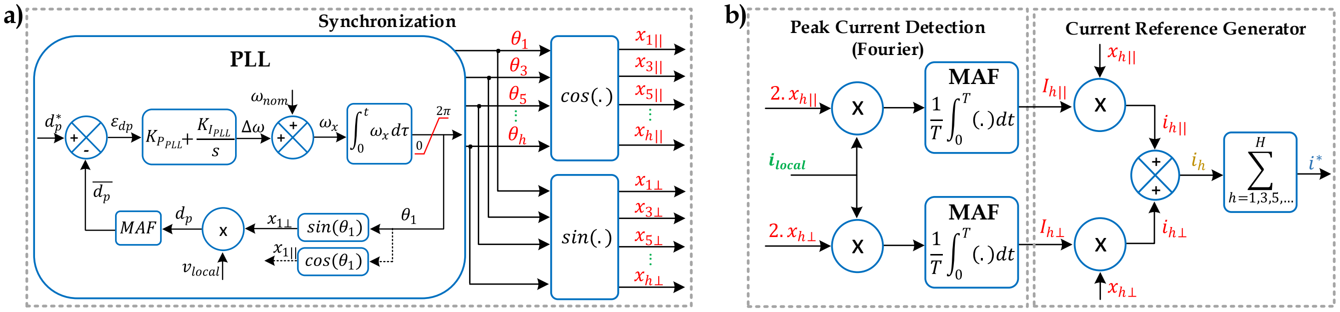

Fig. 2. Harmonic detection algorithm in time domain: (a) PLL-based synchronization algorithm and (b) peak detector and selective current reference generator.

The current terms can be restored to time-domain signals (i.e., sinusoidal waveforms) by means of (1):

$$i_{h\parallel} = I_{h\parallel} \cdot x_{h\parallel} \tag{1.a}$$

$$i_{h\perp} = I_{h\perp} \cdot x_{h\perp} \tag{1.b}$$

where $i_{h\parallel}$ and $i_{h\perp}$ are orthogonal to each other. Eventually, the current reference for the selective harmonic compensation is calculated as:

$$i^* = \sum_{h=3,5,7,\cdots}^{H} i_h = \sum_{h=3,5,7,\cdots}^{H} (i_{h\parallel} + i_{h\perp}) \tag{2}$$

For distributed operation, the PLL algorithm and the peak current detector shown in Fig. 2(a) and Fig. 2(b) is implemented locally in both the CC and in the EGs. Instead, the current reference generator shown in Fig. 2(b) is implemented only in the distributed units. Note that, although harmonic decomposition is performed herein on the basis of [36] and Fig. 2, any other methodology [37,38] might be used at this stage for the detection of current terms.

2.4. Aspects of the communication infrastructure

Modern MGs typically feature advanced automation and communication infrastructures, as well as distributed electronic converters with control capabilities, which allows the application of the CBC methodology and supports the required low-bandwidth communication between the CC and EGs. The related communication can exploit many protocols that can ensure a limited bit rate for sending and receiving data [39]. Notably, similar communication performances should be met for a proper interconnection and interoperation of inverters as defined by contemporary standards (see, e.g., the IEEE Std. 1547-2018 [31]).

An example of suitable technology to broadcast the control signals from the CC to the EGs is the SunSpec Modbus protocol [40] that has been incorporated within [31]. This technology allows inverters to use low data-rate communication, comprising narrowband transmission with baud rates from 9600 bps to 115,200 bps [41], which easily fulfills the data transfer requirements to perform the CBC algorithm considering networks such as shown in [32]. While maximum latencies of 100 ms can be fulfilled by modern communication systems [42], such aspects bring correspondingly slower response times during transients but do not impair the stability of the CBC operation, as shown in Section 4, Section 5.5 and Section 5.6.

3. Active, reactive, and harmonic current sharing through Current-Based control

The main goal of the CBC is to provide proper current references for distributed SPIs to make them coordinately share the active, reactive, and harmonic currents – resulting from the network and the PCC needs – according to their maximum current generation capability. Fig. 3 shows the considered MG structure using the CBC strategy; the proposed secondary layer controller performs as follows.

3.1. Gathering of local data packets

The n-th SPI sends to the CC a data packet composed of the terms $I_{h\parallel}^{fn}$ and $I_{h\perp}^{fn}$, which were introduced in Section 2, as well as the maximum active current available from its primary source I_{max}^{fn}, and its nominal current capacity I_{nom}^{fn}.

3.2. CBC processing at the CC

The CBC strategy is processed at the CC upon the beginning of each new control cycle k, which occurs periodically according to the needs of the MG, and based on the capability of the communication infrastructure required to coordinate the distributed EGs. The control cycle is updated (i.e., $k = k + 1$) when a new control window begins. Herein,

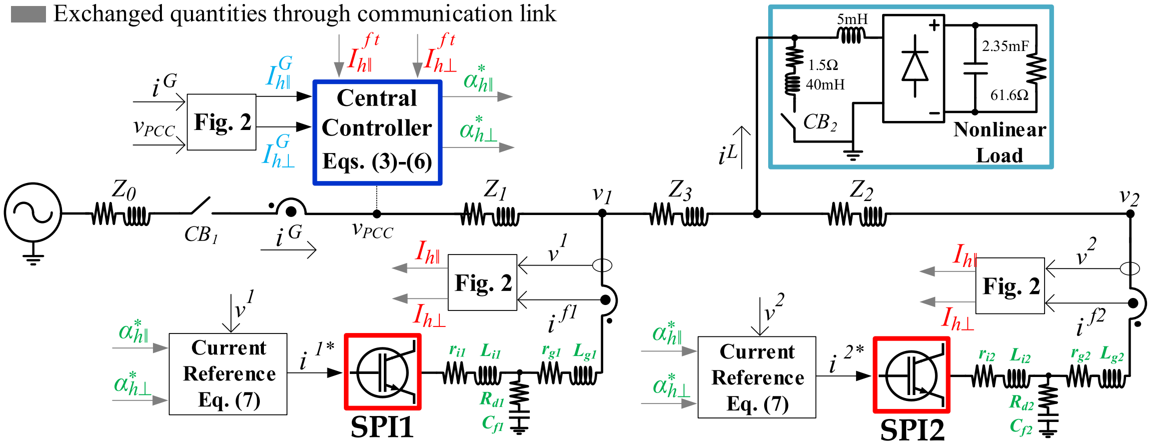

Fig. 3. Microgrid topology adopted for simulations and experimental validation of the CBC strategy.

the term control window identifies the time interval that elapses between successive sessions of data gathering, processing, and communication to the distributed SPIs, being executed at a specific frequency, f_{CBC}, defined by the CC's digital processor. As soon as all the SPIs' data packets are collected (i.e., $n = 1 \ldots N$), the CC calculates the total contribution of each distributed unit in terms of injected current and the total nominal capability of the installed SPIs. The cumulative (i.e., total) quantities, denoted by superscript "t", at the k-th control cycle are:

$$I_{h\parallel}^{ft}(k) = \sum_{n=1}^{N} I_{h\parallel}^{fn}(k) \tag{3.a}$$

$$I_{h\perp}^{ft}(k) = \sum_{n=1}^{N} I_{h\perp}^{fn}(k) \tag{3.b}$$

$$I_{max}^{ft}(k) = \sum_{n=1}^{N} I_{max}^{fn}(k) \tag{3.c}$$

$$I_{nom}^{ft}(k) = \sum_{n=1}^{N} I_{nom}^{fn}(k) \tag{3.d}$$

Then, the CC measures the voltage and current at the PCC and determines the in-phase ($I_{h\parallel}^{G}$) and quadrature ($I_{h\perp}^{G}$) grid peak currents at harmonic order h. On the basis of these quantities and Kirchhoff's current law, the load current is calculated. According to the notation in Fig. 3, it yields:

$$I_{h\parallel}^{L}(k) = I_{h\parallel}^{G}(k) + I_{h\parallel}^{ft}(k) \tag{4.a}$$

$$I_{h\perp}^{L}(k) = I_{h\perp}^{G}(k) + I_{h\perp}^{ft}(k) \tag{4.b}$$

The SPIs contribution to the MG in the next control cycle $k + 1$, that is, the in-phase ($I_{h\parallel}^{*}(k + 1)$) and quadrature ($I_{h\perp}^{*}(k + 1)$) peak current terms, is determined based on the desired current circulation at the PCC, that is, the in-phase ($I_{h\parallel}^{G*}$) and quadrature ($I_{h\perp}^{G*}$) peak currents, as in (5). Note that I_{h}^{G*} is set by the tertiary control level, and the estimated quantities for the next control cycle $k + 1$ are based on the quantities measured during the last control cycle k.

$$I_{h\parallel}^{*}(k+1) = I_{h\parallel}^{L}(k) - I_{h\parallel}^{G*}(k+1) \tag{5.a}$$

$$I_{h\perp}^{*}(k+1) = I_{h\perp}^{L}(k) - I_{h\perp}^{G*}(k+1) \tag{5.b}$$

Finally, the current commands $\alpha_{h\parallel}$ and $\alpha_{h\perp}$, both ranging in the interval $[-1, 1]$, are computed and broadcasted to all the distributed SPIs. The in-phase current terms are controlled by variable $\alpha_{h\parallel}$, while the quadrature current terms are controlled by variable $\alpha_{h\perp}$. These coefficients are defined as:

$$\alpha_{h\parallel}^{*} = \frac{I_{h\parallel}^{*}(k+1)}{\sqrt{\Delta I}}, \quad -1 \le \alpha_{h\parallel}^{*} \le 1 \tag{6.a}$$

$$\alpha_{h\perp}^{*} = \frac{I_{h\perp}^{*}(k+1)}{\sqrt{\Delta I}}, \quad -1 \le \alpha_{h\perp}^{*} \le 1 \tag{6.b}$$

where the actual current capability (ΔI) is calculated sequentially to avoid overcurrent, as seen in Pseudocode 1. Note that ΔI describes the availability of peak current to be considered for the calculation of each α_{h}^{*} term, starting from $\Delta I = I_{nom}^{ft^2}$ and being reduced considering orthogonal subtractions after the allocation of each in-phase and quadrature harmonic term.

It is worth remarking that the proposed sequential algorithm considers harmonics of increasing order h, giving priority to the in-phase component over to quadrature component. Accordingly, the in-phase component of the fundamental (i.e., $h = 1$), which determines active power flow, is considered first, giving $\alpha_{1\parallel}$. Then, coefficient $\alpha_{1\perp}$ associated to the reactive power flow is computed on the basis of the remaining available capacity $\Delta I = I_{nom}^{ft^2} - I_{1\parallel}^{ft^2}$ (see line 20 of Pseudocode 1). All the harmonics of higher order are considered, sequentially, in the same way, giving, $\alpha_{3\parallel}$, $\alpha_{3\perp}$, $\alpha_{5\parallel}$, $\alpha_{5\perp}$, $\alpha_{7\parallel}$, $\alpha_{7\perp}$, up to the chosen maximum harmonic term H. Nonetheless, the CBC is easily adapted for attending any logic of current terms priority.

The coefficients can be positive or negative, to represent, respectively, generated or absorbed active power by the SPIs (for what concerns $\alpha_{1\parallel}$) and inductive or capacitive reactive power injected by the SPIs (for what concerns $\alpha_{1\perp}$). Of course, for EGs without energy storage $\alpha_{1\parallel}$ must assume only positive values and, analogously, SPIs implementing APFs neglect the coefficient $\alpha_{1\parallel}$ (i.e., $I_{max}^{fn} = 0$). These constraints are suitably managed by the control scheme by properly defining the bounds in (6). Besides, the coefficients hold for the coordination of distributed SPIs in both grid-connected and islanded operation.

Pseudocode 1 (*CBC algorithm at the CC*).

```
1: function CURRENTBASEDCONTROL (Eqs. (3), (4), (5))
2:   for $h \leftarrow 1$ to $H$ do          ("←" means assignment from right to left)
3:     if $h = 1$ then
4:       $\Delta I \leftarrow I_{max}^{ft}$
5:       if $\Delta I > 0$ then
6:         $\alpha_{1\parallel} \leftarrow$ Eq. (6.a) & Saturate if $< -1$ or $> 1$
7:       else
8:         $\alpha_{1\parallel} \leftarrow 0$
9:       end if
10:      $\Delta I \leftarrow I_{nom}^{ft^2} - I_{max}^{ft^2}$
11:      goto Line 20
12:    else
13:      $\Delta I \leftarrow \Delta I - I_{(h-2)\perp}^{ft^2}$
14:      if $\Delta I > 0$ then
15:        $\alpha_{h\parallel} \leftarrow$ Eq. (6.a) & Saturate if $< -1$ or $> 1$
16:      else
17:        $\alpha_{h\parallel} \leftarrow 0$
18:      end if
19:    end if
20:    $\Delta I \leftarrow \Delta I - I_{h\parallel}^{ft^2}$
21:    if $\Delta I > 0$ then
22:      $\alpha_{h\perp} \leftarrow$ Eq. (6.b) & Saturate if $< -1$ or $> 1$
23:    else
24:      $\alpha_{h\perp} \leftarrow 0$
25:    end if
26:    GATHERCONTROLCOMMANDS ($\alpha_{h\parallel}$, $\alpha_{h\perp}$)
27:    $h \leftarrow h + 2$
28:  end for
29:  DISPATCHCONTROLCOMMANDS ()
30: end function
```

3.3. SPI's local current reference setting

Using the current commands dispatched by the CC, each SPI generates its own current reference based on its current rating and measured local voltage as:

$$i^{n*} = \sum_{h=1,3,5,7,\ldots}^{H} (\underbrace{\alpha_{h\parallel}^{*} \cdot \sqrt{\Delta I^{n}}}_{I_{h\parallel}^{fn}}) \cdot x_{h\parallel}^{n} + (\underbrace{\alpha_{h\perp}^{*} \cdot \sqrt{\Delta I^{n}}}_{I_{h\perp}^{fn}}) \cdot x_{h\perp}^{n} \tag{7}$$

Likewise, the actual current capability of each SPI (ΔI^{n}) must be recalculated sequentially, after allocating each current term.

As a final remark, Fig. 3 displays with grey arrows the quantities transferred by communication between the SPIs and the CC; notably, a limited amount of data transfer involving few average quantities (i.e., $\alpha_{h\parallel}^{*}$, $\alpha_{h\perp}^{*}$, $I_{h\parallel}^{fn}$, $I_{h\perp}^{fn}$, I_{max}^{fn}, I_{nom}^{fn}) for each SPI is required. Moreover, the communication is non-critical because temporary and local faults do not impair the basic and specific functions of the primary control. As addressed later by simulation and experimental results, primary layer control may neglect the secondary controller under faults or ineffective communication channels, maintaining SPIs under safe and appropriate operation.

3.4. Current sharing control limitations

It is worth remarking that, in general, node voltages can be phase shifted with respect to the voltage at the PCC due to current circulation through line impedances. Although this condition is not common in the considered low-voltage network scenario [32], it might occur in networks with long cables presenting high X/R ratios. To better describe the issue, let us consider the voltage at the PCC as the voltage reference, corresponding to a cosine function with phase 0°, and the voltage at the generic n-th node of the grid represented as a cosine voltage phase-shifted by θ_n° with respect to the PCC. Based on (7), the SPI current reference can be rewritten as:

$$i^{n*} = \sum_{h=1,3,5,7,\cdots}^{H} [(\alpha^*_{h\parallel}\cdot\sqrt{\Delta I^n})\cdot\cos(h\omega t + h\theta_n^\circ) + (\alpha^*_{h\perp}\cdot\sqrt{\Delta I^n})\cdot\sin(h\omega t + h\theta_n^\circ)] \tag{8}$$

Notably, the current terms in (8) include a voltage phase shift with respect to the PCC, which represents an error term increasing proportionally with the harmonic order ($h\theta_n^\circ$). This term introduces a coupling between the in-phase and quadrature components of the control coefficients and the grid current at the PCC, I^G. For this reason, the system damping ratio decreases as θ and h increase, which may cause resonances in the vicinity of the system natural frequency. However, the error due to these voltage phase shifts is typically small and its effect is compensated at the CC by the feedback of current terms sent through the communication link. Also, inherit system errors (e.g., measurement devices errors) are compensated by the CC. If voltage phase shifts were a concern, they could be overcome by employing low-cost synchrophasor measurement units in the considered LV network, or GPS like approaches [15]. This would allow distributed units to inject current terms with negligible angle deviations with respect to the voltage at the PCC, which would guarantee adequate damping and stability in whatever operating condition. However, it is worth mentioning that voltage phase shifts are usually small in LV MGs with high R/X ratios [3].

Finally, it is remarked that this proposal differs from the methods presented by Akagi *et al.* [43,44] for damping purposes, which are based on voltage detection and closed loop strategy at each distributed unit. In the proposed CBC, harmonic compensation is performed based on current detection and closed loop control at PCC. Since in [43,44] harmonics are dealt with locally, obtaining harmonic reduction at PCC is a side-effect of the local harmonic damping, and the effect of voltage phase deviations among nodes is not considered. From this standpoint, further studies are needed to compare the two proposals in terms of performance, stability, and robustness against the whack-a-mole effect [45].

4. Stability analysis

In this section an overall analysis of the CBC strategy is provided in regard of the closed-loop system stability, while also considering the matter of time delays. The simplified block diagram of Fig. 4 summarizes the main features of the proposed centralized coordinated control, being devised for the concern of active current injection (i.e., in-phase fundamental active current). Similar schemes can be derived for the fundamental quadrature term, as well as for all the other considered harmonic components, since the CBC takes into consideration that all current terms are decoupled; therefore, independently affecting stability. Moreover, harmonic current parcels are only treated through magnitude terms and are never considered over the bandwidth of local controllers. On the other hand, time delays are inherent to the CBC approach, therefore, they are considered on the following analysis to take into account possible phase margin deviations.

The scheme in Fig. 4 comprises the CC, the communication infrastructure, EGs' local controllers and the considered power system infrastructure. As mentioned before, the CBC is processed with a periodic frequency, f_{CBC}, leading to a processing time of $T = 1/f_{CBC}$, which is used to attain the discrete transfer function of the system between the total absorbed current, $I^L_{1\parallel}$, and the control reference, $I^*_{1\parallel}$, given by (9). Herein, the time-delay existing due to the communication infrastructure is described as T_D, and ω_c is the bandwidth of the local controllers existing on the EGs, which is approximately 1200 Hz (i.e., $\omega_c = 2.\ \pi.\ 1200$ rad/s). Where z is defined as the discrete operator and H_{ω_c} is the transfer function of the local controllers. Hence, the overall system stability is analyzed by two cases based on variations of *i*) the time-delay, T_D, and *ii*) the CBC processing time, T.

$$I^*_{1\parallel}(z) = \frac{I^L_{1\parallel}(z)}{z + H_{\omega_c}(z).\ T_D(z).\ [1 - T_D(z)]} \tag{9}$$

In Fig. 5 the mapping of the poles ("×") and zeros ("○") of the system is presented for the two previous cases intended, considering: *i*) T_D varying from 1/600 s up to 1/6 s, with T equal to 1/60 s, and *ii*) with constant $T_D = 1/60$ s and T varying from 1/600 s up to 1/6 s. Firstly, under a generalized analysis, it can be promptly seen that T_D and T present different impact on system stability. Since the dynamic of the CBC relies on knowing the actual status of currents being injected by EGs before dispatching control commands, it is expected for the former case to present a more significant variation in behavior as SPIs' packets take more time to arrive at the CC.

When it comes to the first case, comprising variations of T_D, one can note in Fig. 5(a) that the system is stable for all the considered time-delays, since all the poles lie inside the unit circle. Hence, by considering the aforementioned scenario of maximum latency of about 100 ms [42], the CBC operation would not impair system stability. In addition, such poles tend to move towards the positive real axis and to become more dominant. This is also reasonable, because as T_D increases, the CBC response takes more time to respond to transients in the power system, as further discussed in the following section. Yet, although the zeros of the system do not affect stability by being outside the unit circle, they potentially introduce non-minimum phase features, which may limit control bandwidth and decrease the phase margin [46].

Finally, for the case in which T varies, depicted in Fig. 5(b), the poles of the system also do not lay outside the unit circle, indicating that stability is maintained for the considered timing. Nonetheless, they tend to slightly move towards the negative real axis, which indicates likely oscillatory behaviors for the system [46]. This is an interesting and reasonable result due to the fact that the time response of the system is directly dependent on the time to process, update, and

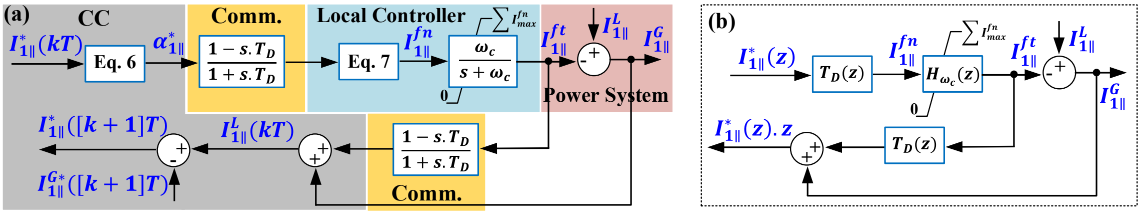

Fig. 4. Simplified control model of the CBC strategy used for stability analysis.

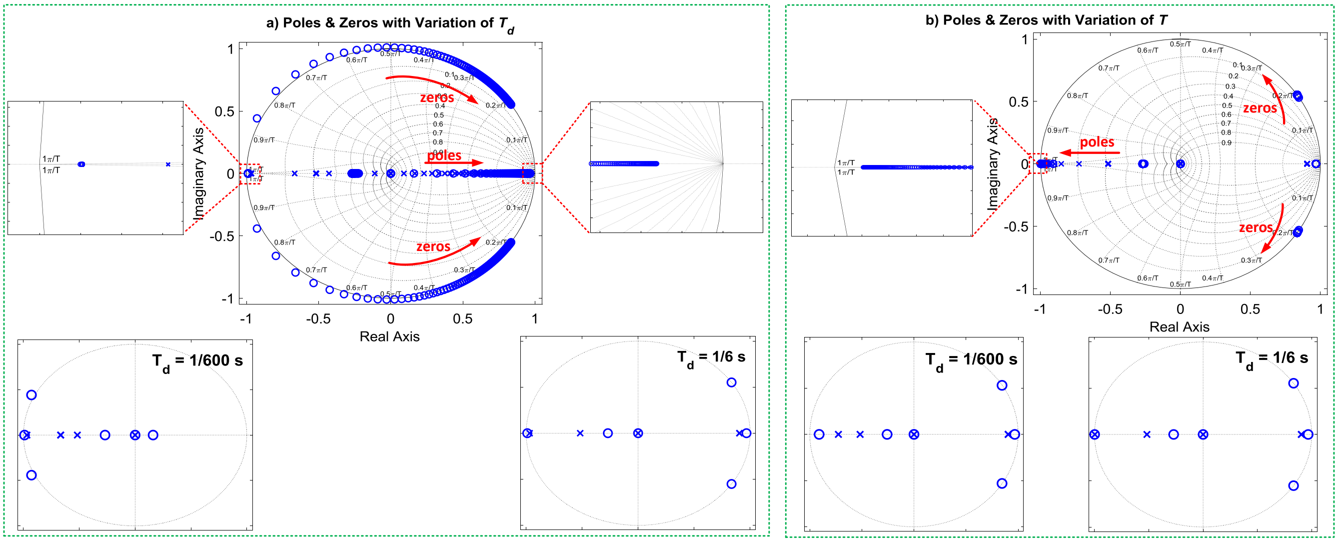

Fig. 5. Pole and zero mapping for the stability analysis of the CBC strategy considering variation of (a) T_D and (b) T.

transmit the control coefficients calculated by the CBC.

5. Experimental and simulation results of current sharing in a Low-Voltage microgrid

Experimental and simulation results showing the accurate sharing of active, reactive, and harmonic currents achievable by the CBC and its capability of distributedly and selectively compensating harmonics are reported in this section, considering:

- Case study 1, showing selective current sharing under sinusoidal grid voltage condition, comprising load step variations, limited current capability, and active power flow control at the PCC (experimental result);
- Case study 2, showing current sharing under cable impedance variations, abnormal voltage conditions (i.e., sags and swells), and connection of extra SPIs (simulation result);
- Case study 3, showing selective current sharing under heavily distorted grid voltage and bidirectional power flow control at the MG PCC (simulation result);
- Case study 4, showing the impact of communication loss on the operation of the CBC algorithm and its effect on MG stability (simulation and experimental result);
- Case study 5, showing different conditions of data packet delays and how it interferes on the local control of EGs and on the overall performance of the CBC algorithm (experimental result).

Each case study has been evaluated by PSIM simulations and experimentally, referring to the system displayed in Fig. 3.

5.1. Microgrid testbed and SPI control design parameters

The implemented MG testbed for the experimental verification is visible in Fig. 6, its parameters are summarized in Table 1. It consists of *i)* a 60 Hz AC power source, which is devised by a real connection with the local utility, that can be disconnected from the MG (islanded mode) through a circuit breaker (CB_1); *ii)* a nonlinear load composed of a diode rectifier feeding, at its DC side, a capacitor (C = 2.35 mF) in parallel with a resistor (61.6 Ω), and fed through an inductor (L = 5 mH) at the AC side, *iii)* parallel RL load (1.5 + j15.07 Ω) that can be switched on and off by a circuit breaker (CB_2); *iv)* two single-phase full-bridge SPIs, with SKM 75GB128D IGBT modules equipped with output LCL filters with passive

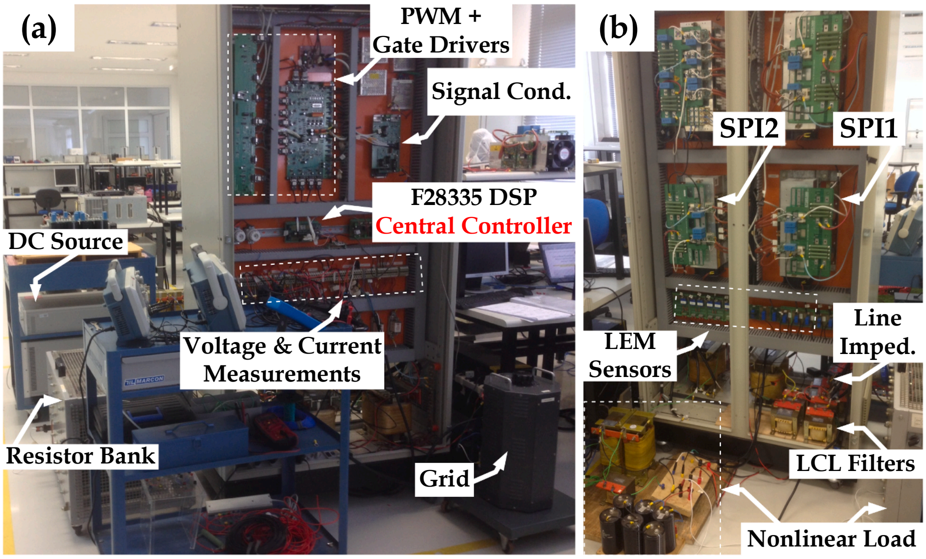

Fig. 6. Experimental testbed: (a) front view; (b) back view.

Table 1
Parameters of Microgrid Tested and Distributed SPIs.

Feature	Specification
Grid nominal voltage (V_{grid}) and frequency (f_{grid})	127 V – 60 Hz
Lines Impedances* ($Z_0 = Z_1 = Z_2 = Z_3$)	0.020 + j0.188 Ω
SPI$_1$ Nominal Peak Current (I_{nom}^{f1})	12 A$_{pk}$
SPI$_2$ Nominal Peak Current (I_{nom}^{f2})	8 A$_{pk}$
SPIs DC Link Voltage ($V_{DC1} = V_{DC2}$)	235 V
LCL Filter SPI Side Inductors ($L_{i1} = L_{i2}$)	1.0 mH
LCL Filter Grid Side Inductors ($L_{g1} = L_{g2}$)	1.0 mH
LCL Filter Capacitors ($C_{f1} = C_{f2}$)	3.3 µF
LCL Filter Damping Resistors ($R_{d1} = R_{d2}$)	2.5 Ω
Current Sensor Gain (Ki)	1/20
SPIs Switching Frequency (f_{sw})	12 kHz
Sampling Frequency (f_s)	12 kHz
PR Controllers Proportional Gain (KP_i)	0.90 pu
PR Controllers Integrator Gain (KI_h)	132 pu

* Resistive feature adopted on simulations: $Z_0 = Z_1 = Z_2 = Z_3 = 0.1 + j0.02\,\Omega$.

damping [47] and supplied by programmable DC power sources; *v)* interconnecting line impedances as shown in Table 1.

Current regulators for the inner control loops of the SPIs are proportional-resonant (PR) controllers, with the gains shown in Table 1, calculated as explained in [48]. The PR controllers were tuned to the fundamental, 3rd, 5th, and 7th harmonic orders. The designed cut-off frequency is $f_c = f_{sw}/10$, phase margin $phm = 60°$, and a three-level PWM strategy is implemented. A floating-point digital signal processor (DSP) TMS320F28335 by *Texas Instruments* is employed for digital controls. *LEM LV25-p* and *LA55-p* sensors are used for voltage and current measurements, respectively. The instruments *DPO3014 Tektronix* oscilloscope and *DPO3PWR Power Analysis Module* were used to collect and analyze the system behavior. As displayed in Fig. 6 and Fig. 7, only one DSP is used for MG initialization, control the current of the two SPIs, and execute the CBC algorithm, for two EGs and one CC. Communication-related issues, like delays and data packet loss, are further discussed in the two dedicated case studies of Section 5.5 and Section 5.6.

At nominal conditions, the apparent power drawn by the load is 1.36 kVA, with power factor of 0.36, total current harmonic distortion (THD$_i$) of 23.25%, and phase displacement of −70.40°, with respect to the PCC voltage. The periodic communication transmission rate (between CC and EGs, and *vice-versa*) is set to a period of the fundamental grid voltage (i.e., $f_{CBC} = 16.67$ ms), for the sake of presentation clarity. Although such transmission rate is realizable [49] for the adopted MG scenario as earlier discussed, the CBC in a real application can limit the frequency of the operational control window considering one of the following two approaches: *i)* the worst scenario of delays, which is given by the slowest EG participating on current sharing; or *ii)* dynamically adjust the frequency of the CBC control window based on strategies of networked control systems (NCSs), such as time delay and packet loss prediction through robust, predictive, or state feedback control methods [50–52]. Since the former alternative is more critical (i.e., having the CBC strategy to assume the slowest frequency response), it is adopted herein aiming at demonstrating that, even under this condition, MG stability is not affected, Thus, the CBC allows to accommodate the coordination of all EGs, considering delays, as presented in Section 5.5 and 5.6.

5.2. Case study 1: Selective current sharing

In this case study, the experimental behavior of the CBC is presented in Fig. 8 considering different targets ($I_{h\|}^{G*}$) set by the tertiary control level for the current exchanged with the mains.

First, Fig. 8(a) shows the current flowing through the PCC with the SPIs switched off, which is equal to the current absorbed by the nonlinear load. The CB$_2$ is always closed, unless otherwise stated. Fig. 9(a) reports the main spectral components of the PCC current in this condition: the fundamental component ($I_1^G = 9.64$ A$_{RMS}$), the third ($I_3^G = 1.79$ A$_{RMS}$), and fifth ($I_5^G = 0.64$ A$_{RMS}$) harmonics. In the following paragraphs, the CBC algorithm is set to selectively cancel these components, sharing the compensation effort in proportion to the SPI current capabilities ($r_{SPIs} = I_{nom}^{f1}/I_{nom}^{f2} = 1.5$).

In Fig. 8(b) the CBC is set to deal with just the fundamental component, which is crucial to support MG dispatchability. In this condition, the CC sends to the distributed SPIs current signals ($\alpha_{1\|}$, $\alpha_{1\perp}$) that are computed to adjust to zero the active and reactive currents flowing at the PCC. Fig. 9(b) reveals a small residual fundamental component, of magnitude $I_1^G = 0.17$ A$_{RMS}$, while the other harmonic magnitudes are nearly not affected. The proportionality ratio contribution of SPIs is also respected, being $r_{SPIs} = 1.49$.

Fig. 8(c)-(d) show the capability of the CBC algorithm of compensating just reactive [Fig. 8(c)] and the 3rd and 5th harmonic components [Fig. 8(d)]. This is a relevant operation mode, considering that the local source of power may be not always available due to the characteristic intermittency shown by renewables, still, SPIs can provide the service of distributedly compensating unwanted reactive and harmonic currents. Referring to Fig. 8(c), $I_{1\perp}^G$ is regulated to zero, resulting in a significant reduction of the fundamental magnitude ($I_1^G = 3.38$ A$_{RMS}$), as reported in Fig. 9(c), resulting in I_1^G with THD$_i$ = 63.5% and practically zero phase ($ph = 1.94°$). The measured repartition ratio among SPIs is $r_{SPIs} = 1.49$. Referring to Fig. 8(d), Fig. 9(d) shows that the considered 3rd and 5th harmonics are suppressed ($I_3^G = 0.06$ A$_{RMS}$, $I_5^G = 0.06$ A$_{RMS}$), resulting in a less distorted PCC current (THD$_i$ = 4.71%). A proportional sharing is obtained also in this case ($r_{SPIs} = 1.45$).

Fig. 8(e) refers to the case of total compensation of the active ($I_{1\|}^G$), reactive ($I_{1\perp}^G$), 3rd (I_3^G), and 5th (I_5^G) components at PCC. Now, $r_{SPIs} = 1.48$. Fig. 8(e) shows a tremendous reduction of the targeted components with respect to the initial situation in Fig. 9(a).

In Fig. 8(f), the CBC algorithm robustness is tested upon a load step variation in the MG, caused by the opening of CB$_2$. The CBC periodic data exchange rate is here set to 16.67 ms; after such amount of time, the algorithm succeeds in making the SPIs rapidly adapt to the new

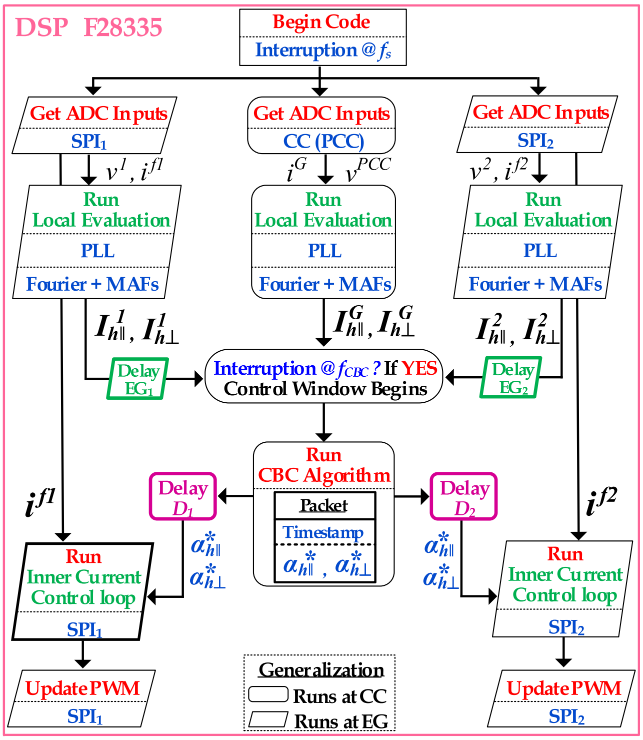

Fig. 7. Control logic implemented on the F28335 DSP.

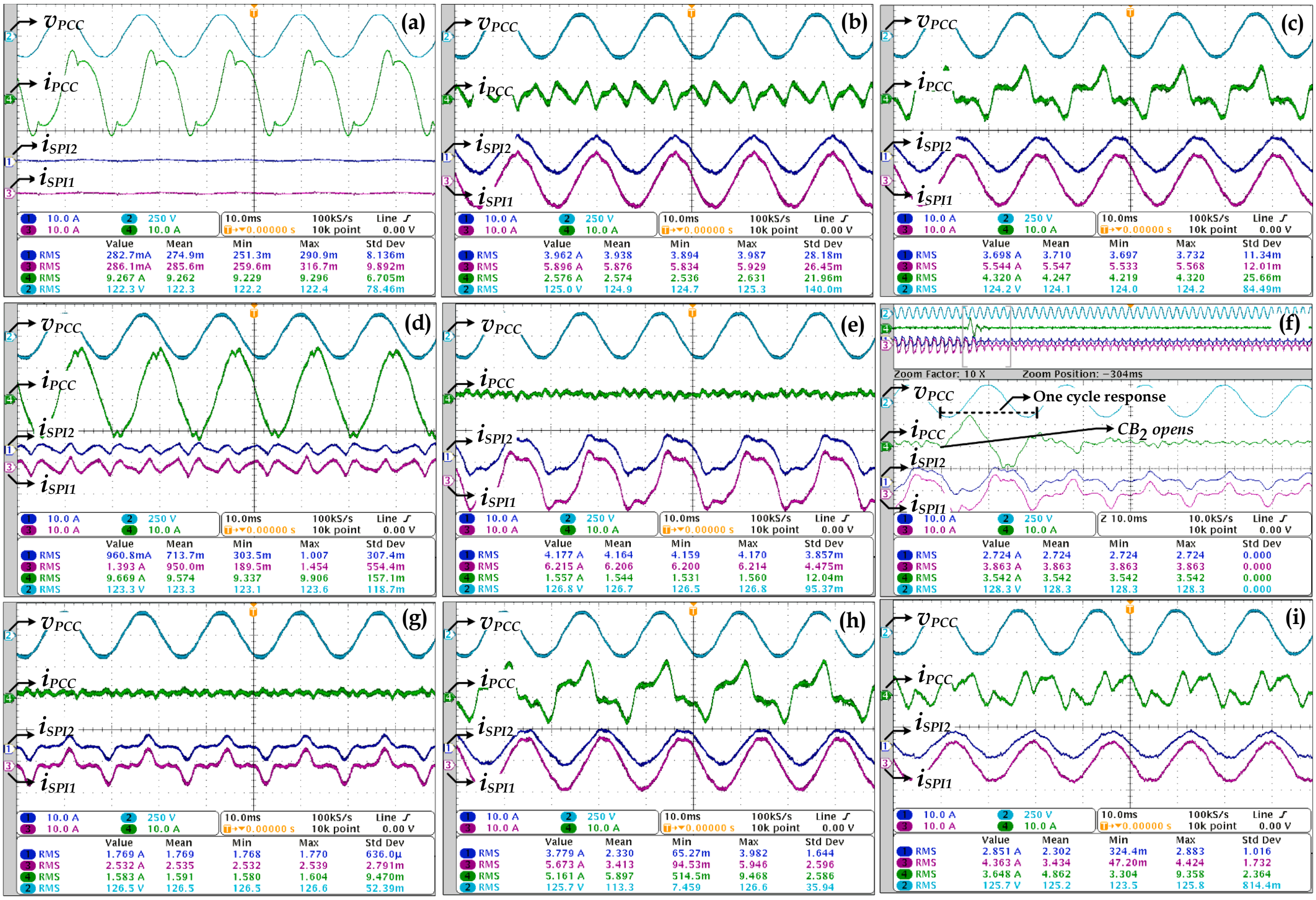

```
(a)      Value    Mean     Min      Max      Std Dev
1 RMS    282.7mA  274.9m   251.3m   290.9m   8.136m
3 RMS    286.1mA  285.6m   259.6m   316.7m   9.892m
4 RMS    9.267 A  9.262    9.229    9.296    6.705m
2 RMS    122.3 V  122.3    122.2    122.4    78.46m

(b)      Value    Mean     Min      Max      Std Dev
1 RMS    3.962 A  3.938    3.894    3.987    28.18m
3 RMS    5.896 A  5.876    5.834    5.929    26.45m
4 RMS    2.576 A  2.574    2.536    2.631    21.96m
2 RMS    125.0 V  124.9    124.7    125.3    140.0m

(c)      Value    Mean     Min      Max      Std Dev
1 RMS    3.698 A  3.710    3.697    3.732    11.34m
3 RMS    5.544 A  5.547    5.533    5.568    12.01m
4 RMS    4.320 A  4.247    4.219    4.320    25.66m
2 RMS    124.2 V  124.1    124.0    124.2    84.49m

(d)      Value    Mean     Min      Max      Std Dev
1 RMS    960.8mA  713.7m   303.5m   1.007    307.4m
3 RMS    1.393 A  950.0m   189.5m   1.454    554.4m
4 RMS    9.669 A  9.574    9.337    9.906    157.1m
2 RMS    123.3 V  123.3    123.1    123.6    118.7m

(e)      Value    Mean     Min      Max      Std Dev
1 RMS    4.177 A  4.164    4.159    4.170    3.857m
3 RMS    6.215 A  6.206    6.200    6.214    4.475m
4 RMS    1.557 A  1.544    1.531    1.560    12.04m
2 RMS    126.8 V  126.7    126.5    126.8    95.37m

(f)      Value    Mean     Min      Max      Std Dev
1 RMS    2.724 A  2.724    2.724    2.724    0.000
3 RMS    3.863 A  3.863    3.863    3.863    0.000
4 RMS    3.542 A  3.542    3.542    3.542    0.000
2 RMS    128.3 V  128.3    128.3    128.3    0.000

(g)      Value    Mean     Min      Max      Std Dev
1 RMS    1.769 A  1.769    1.768    1.770    636.0µ
3 RMS    2.532 A  2.535    2.532    2.539    2.791m
4 RMS    1.583 A  1.591    1.580    1.604    9.470m
2 RMS    126.5 V  126.5    126.5    126.6    52.39m

(h)      Value    Mean     Min      Max      Std Dev
1 RMS    3.779 A  2.330    65.27m   3.982    1.644
3 RMS    5.673 A  3.413    94.53m   5.946    2.596
4 RMS    5.161 A  5.897    514.5m   9.468    2.586
2 RMS    125.7 V  113.3    7.459    126.6    35.94

(i)      Value    Mean     Min      Max      Std Dev
1 RMS    2.851 A  2.302    324.4m   2.883    1.016
3 RMS    4.363 A  3.434    47.20m   4.424    1.732
4 RMS    3.648 A  4.862    3.304    9.358    2.364
2 RMS    125.7 V  125.2    123.5    125.8    814.4m
```

Fig. 8. Experimental results of the CBC operation under sinusoidal voltage condition and CB$_2$ closed. (a) no control (i.e., SPIs switched off); (b) fundamental active and reactive power control with zero reference; (c) fundamental reactive power control, no active power control; (d) 3rd and 5th harmonic compensation, no active or reactive power control; (e) fundamental active and reactive power control plus 3rd and 5th harmonic compensation; (f) CB$_2$ opens in the situation of (e); (g) steady-state after the transient in (f); (h) fundamental active and reactive power control plus 3rd and 5th harmonic compensation with $I_{1\parallel}^{G} = 6$A; (i) operation under limited power capacity from distributed energy resources.

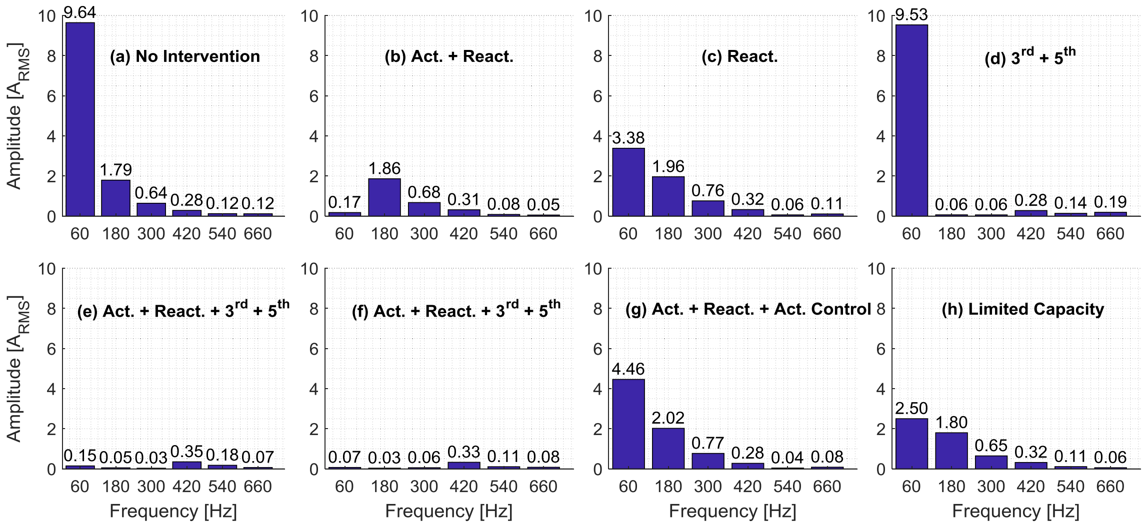

Fig. 9. Harmonic spectrum of the measured PCC current on each of the experimented cases shown in Fig. 8.

operation regime, avoiding any SPI overcurrents. The new steady-state condition is displayed in Fig. 8(g), where it is possible to notice that the active, reactive, 3rd and 5th harmonic orders sharing is maintained. The PCC current harmonics analysis is reported in Fig. 9(f). The proportionality ratio between the two SPIs is $r_{SPIs} = 1.43$.

To validate the full controllability of steer current to the grid, Fig. 8(h) shows the steady-state behavior with CB$_2$ switched on again, and with active peak current references of $I_{1\parallel}^{G*} = 6$ A$_{\text{pk}}$, $I_{1\perp}^{G*} = 0$ A$_{\text{pk}}$, and $I_h^{G*} = 0$ A$_{\text{pk}}$, for $h = 3$ and$h = 5$. At the secondary controller, the CC processes the respective control commands to proportionally drive the

SPIs according to the CBC, achieving approximately the desired peak value ($I_{1\|}^{G}$ = 6.30 A_{pk}). The resulting PCC current is practically in-phase with the PCC voltage, ph = 2.93°. Also, considering Fig. 9(g), it is possible to notice that the reactive current is compensated while not affecting the magnitude of the other harmonics. Note that, by supplying the active and reactive load currents, along with the active control parcel ($I_{1\|}^{G*}$), the SPIs reach their nominal capacities; thus, not compensating the harmonic terms and resulting in distorted PCC current. In this case, r_{SPIs} = 1.50 and THD_{i} = 48.45%.

Finally, Fig. 8(i) shows the operation under very limited current capacity, that is, the required compensation effort transcends the total SPIs capability. In this case, the SPIs current capabilities are set to, I_{nom}^{f1} = 6 A_{pk}, and, I_{nom}^{f2} = 4 A_{pk}, while the tertiary layer requires zero active ($I_{1\|}^{G}$), reactive ($I_{1\perp}^{G}$), 3rd (I_{3}^{G}) and 5th (I_{5}^{G}) current terms at the PCC. By inspecting Fig. 8(i) it is noticed that the SPIs inject currents with r_{SPIs} = 1.53. As described in Pseudocode 1, in this case the CBC algorithm gives priority to the active fundamental current, followed by the reactive fundamental term and then the in-phase and quadrature harmonic terms. The frequency spectrum reported in Fig. 9(h) proves that the CBC respects the current limits of the SPIs: the active power is provided by the SPIs up to their power limits, while reactive and harmonic terms are left uncompensated. Therefore, the CBC achieves the full exploitation of the available resources while respecting their limitations (i.e., limiting thermal stresses) and properly managing loads needs also if beyond the generation capacity of the distributed resources. In this case, it is noticeable that distorted current remained at the PCC due to the SPIs current saturation, not allowing harmonic compensation. Besides, a fundamental component of I_{1}^{G} = 2.50 A_{RMS} with phase ph = -89.88° still circulated at the PCC, relating to a residual reactive parcel.

5.3. Case study 2: Current sharing under parameters variations

The robustness of CBC with respect to grid parameters variations and uncertainties is now considered. Fig. 10 refers to a simulation model with varying operation conditions, including grid voltage changes, connection of an additional SPI, and line impedance variations. The PSIM simulation uses the instantaneous description of the SPIs used in the experimental section, with the same electrical and control structure and parameters. The power lines used on simulation are $Z_0 = Z_1 = Z_2 = Z_3 = 0.1 + j0.02\,\Omega$.

In Stage #1 the CBC controls SPI_1 and SPI_2 to provide the whole active ($I_{1\|}^{G}$), reactive ($I_{1\perp}^{G}$), and harmonic currents absorbed by the load. For this case, only the 3rd, 5th and 7th harmonics are processed by the primary and secondary layers. Accordingly, the grid current is practically zero (blue curve at the top of Fig. 10). In Stage #2, a voltage swell of 15% of the nominal voltage is applied between 1.03 and 1.10 s. The system smoothly rides through the abnormal event while the CBC keeps on adjusting the control coefficients ($\alpha_{h\|}^{*}$, $\alpha_{h\perp}^{*}$) according to the MG needs and status. The load behaves as a constant impedance.

The nominal grid voltage is restored in Stage #3, where the CBC keeps on smoothly to adequately share the targeted terms without inrush currents. A voltage sag is applied in Stage #4, reducing the grid voltage by 15%. Also in this case, the CBC and SPIs operation shows unperturbed by the power quality issue. In Stage #5, with the voltage restored to nominal values, an additional EG (SPI_3) connected in parallel to the nonlinear load attains permission to take part to the CBC control and starts operation, contributing proportionally to the overall current sharing of the MG. SPI_3 is modeled as the other two SPIs, but it operates under a nominal peak current ofI_{nom}^{f3} = 6 A_{pk}. The expected steady-state operation is attained after a few grid cycles.

Finally, in Stage #6, all the MG's line impedances are changed to $Z_0 = Z_1 = Z_2 = Z_3 = 0.02 + j0.018\,\Omega$ (same value used in the experimental tests), bringing the R/X ratio from 5 to 1.11. It can be noted that the control properly adapts to the new operating condition without suffering from the applied disturbance.

5.4. Case study 3: Current sharing under voltage distortion

The performance of the CBC with a heavily distorted grid voltage is now shown by a simulation comprising five operating conditions. The results are shown in Fig. 11. The grid voltage is assumed to include 25% of 3rd order harmonic, shifted by −30° from the fundamental, that is, $v^G = 179.6\ \cos(2\pi{\cdot}60\,t) + 44.9\ \sin(3{\cdot}(2\pi{\cdot}60\,t\ -\ 30°))$. Power line impedances are set mainly resistive, as in the previously considered scenario.

Simulation starts at Stage #1 with SPI_1 and SPI_2 switched off, to show the operation with loads only (i.e., without the compensation effect given by the CBC). At Stage #2, the active and reactive current sharing is enabled. References $I_{h\|}^{G*}$ and $I_{h\perp}^{G*}$ are set to zero, allowing the circulation of only harmonic currents at the grid side. In Stage #3, the selective harmonic current sharing is enabled. The control is set to make distributed units compensate the 3rd, 5th, and 7th harmonics. Accordingly, the resulting grid current shows just a negligible harmonic content.

Finally, the direct power flow control is set$I_{h\|}^{G*}$ = 8 A_{pk} (active power set-point), also demanding$I_{h\perp}^{G*}$ = 0 A_{pk} (reactive power set-point). Note that the waveform of the grid current (i^G) is practically sinusoidal, with THD_{i} = 3.01%, and in-phase with v^G, even with a distorted grid voltage, with THD_{v} = 25.11%. Thereupon, at 1.2 s, $I_{h\|}^{G*}$is changed to −8 $\text{A}_{\text{pk},}$ inverting the active power flow. This results in

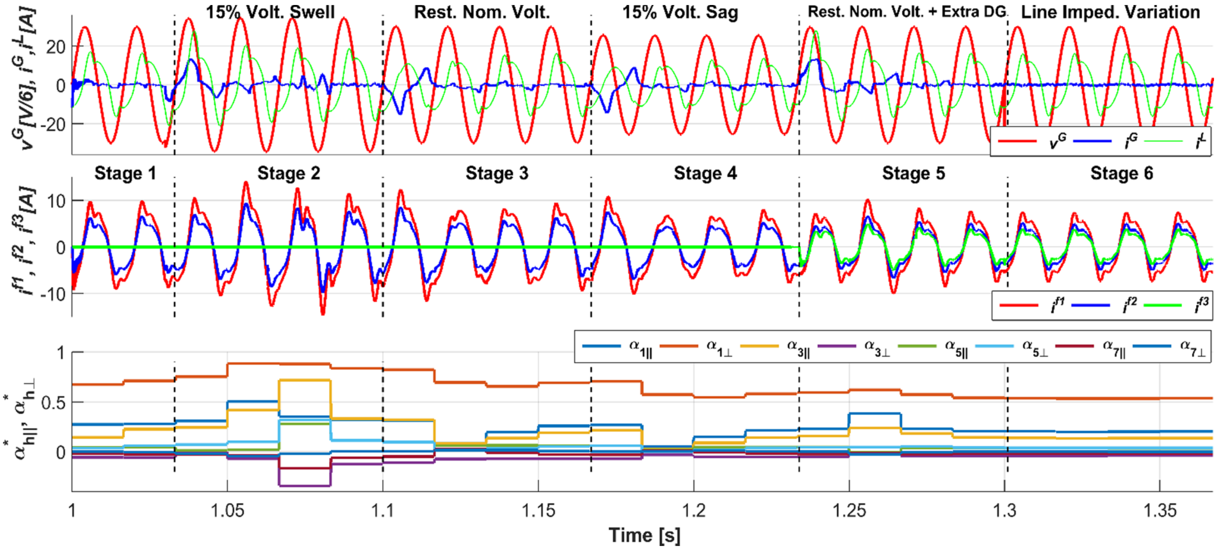

Fig. 10. Simulation results for the CBC under grid parameters variations.

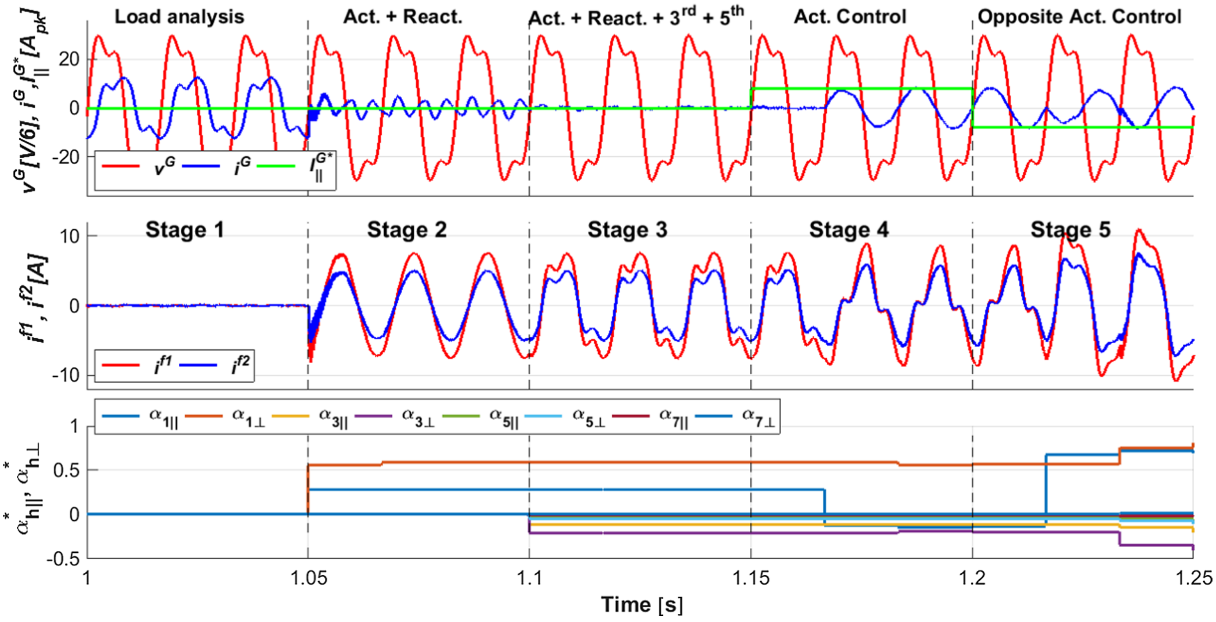

Fig. 11. Simulation results of the CBC under heavily distorted grid voltage.

sinusoidal waveforms with opposite phase for i^G and v^G.

5.5. Case study 4: Operation considering loss of communication

The impact of data transmission issues bringing to packet losses is now assessed. The considered case study shows that the CBC can keep a stable operation even under such faulty conditions.

The simulation and experimental results presented in Fig. 12 are herein used to discuss the issue of communication loss. Such results refer to the same system parameters and experimental setup considered before (i.e., LV MG comprising nonlinear load and two SPIs with parameters given in Section 5.1, but with current sensor gain of $K_i = 1/40$ A). Six operation stages are shown to demonstrate how the system performs when the communication links of any SPIs are under fault, and how the algorithm proceeds when the data transmission links are re-established. Additionally, the consideration of the CC's communication link under fault is evaluated as well. For the sake of easier understanding, the time rate of the CBC control window, and the respective communication rate between CC and EGs, is set to occur once every two fundamental cycles (i.e., f_{CBC} = 33.33 ms). Yet, it is reinforced that only the beginning of some particular control windows are shown in Fig. 12.

A premise of the CBC approach is that it lies on the secondary hierarchical layer, which does not affect the local operation of EGs and the fact that they are ruled locally by their primary layers. This means that, under faults or any other local power issues, the local controllers are responsible for maintaining safe and reliable operation of the SPIs regardless of the secondary layer availability. Thus, considering a hypothetical scenario on which, when driven by just their primary control, the two SPIs are injecting only active power, the first operation interval is shown in Stage #1 in Fig. 12(a). Since the communication link is not active (i.e., "off"), SPIs use only the primary layer controllers to inject the available fundamental active power, which is set to be 6 A$_{pk}$. As a consequence, besides the load current shown in Fig. 8(a) (CB$_2$ is switched on), the PCC current presents fundamental component with higher amplitude due to the active current injection from EGs.

In Stage #2 the communication link is activated, allowing the secondary layer to participate on the operation of the SPIs, and the CBC starts steering EGs to share the load currents. Note that, after the control window occurs (i.e., data collected, processed, and transmitted), the system presents a delay of two fundamental cycles to change the current status due to the new transmission rate adopted, operating similarly to the case discussed in Fig. 8(f). At approximately 1.03 s, SPI$_2$ then detects that its communication link is faulty (see dotted red trace in Stage #2). Since no communication exists, the primary layer of SPI$_2$ takes over control and this EG returns to its basic local operation mode instantaneously (i.e., injecting 6 A$_{pk}$ of active current). This condition is also verified by experiments in Fig. 12(b) and Fig. 12(d). By still having SPI$_1$ active on current sharing, when the next control window occurs, the algorithm adjusts the scaling coefficients disregarding SPI$_2$, which causes EG$_1$ to saturate its current capability (i.e., 12 A$_{pk}$). Therefore, as displayed in Fig. 12(d) and Fig. 12(e), up to its limit, SPI$_1$ injects active current and part of the reactive component drawn by the load, not compensating harmonics, similar to the case in Fig. 8(i).

Stage #3 comprises the continuation of the previous interval, but it shows the reconnection of SPI$_2$'s communication link (see dotted pink trace). Note that SPI$_2$ does not promptly change its current injection, differently from the case when communication is lost. This only happens when the next control window occurs, allowing both EGs to share load currents again, presenting response time also given by the transmission rate (i.e., at each two fundamental cycles), being depicted in Fig. 12(e) and Fig. 12(f). Stage #4 in Fig. 12(a) emulates a condition on which the CC's communication link is faulty, and similar to Stage #2, upon this detection, the SPIs immediately disregard the secondary layer control and return to operation ruled locally as shown in Fig. 12(f). Stage #5 depicts the sequential instants, on which the communication is re-established by the CC next to a CBC control window. The system is able to manage the change in status [see Fig. 12(b) and Fig. 12(g)] and returns to steer EGs adequately just as in Fig. 8(e). Experimental results reinforce the feasibility of the proposed operation method for all the presented communication loss possibilities, not affecting negatively the overall stability of the system.

5.6. Case study 5: Operation considering data packet delays

The impact of data transmission issues bringing to packet delays is now assessed. Also in this case, such considered study shows that the CBC can keep a stable operation. When a new CBC control window starts to process data coming from the EGs, the following four conditions related to packet delays are likely to occur: *i)* delayed data from the CC to EGs (broadcast is halted); *ii)* delayed data from an EG to the

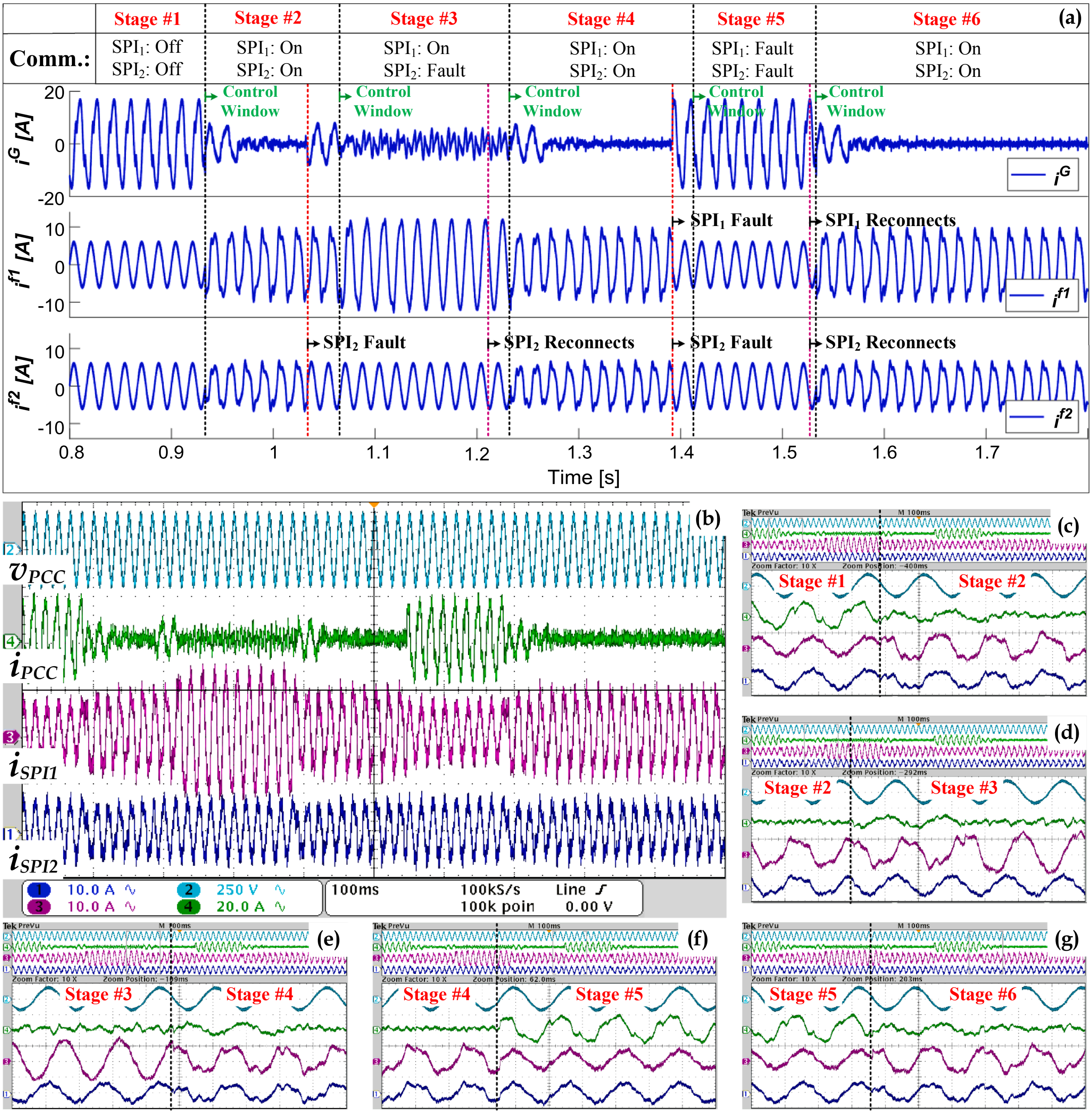

Fig. 12. Simulation and experimental results of the CBC under communication loss. (a) Simulated stages considering communication loss in different instants and with two SPIs sharing currents. (b) Experimental result of the simulated case shown in item (a). (c), (d), (e) (f) and (g): Zoom-in-view of the experimental result in (b), showing the different emulated stages of (a).

CC; *iii)* EGs receiving data with different delays from the CC within the same control cycle (normal operation); and *iv)* EGs receiving data with excessive delays from the CC at different control cycles (unusual operation).

The first two conditions have been previously addressed indirectly. For instance, the case of *i)* can be interpreted as the one depicted in Fig. 8(f) where, after a load step occurs, the control packet from the CC is not immediately sent to the EGs. This means that, if control packets are delayed by *D* to be released from the CC, EGs will just respond slower respective to this same amount of time on which the control packet was hold. In its part, *ii)* is also depicted in Fig. 12(a) between Stages #2 and #3, but now the fault on communication link can be represented by a packet delay from an EG to the CC. If any SPI has its communication link active but its data packet delays to arrive at the CC when the CBC starts a new control cycle (i.e., a new control window begins), that EG will only be considered when the next control cycle starts. Hence, the CBC only considers an EG active for a given control cycle *k* if the respective control packet of that agent arrives in time upon the request of CC.

The remaining cases *iii)* and *iv)* are addressed through the scheme displayed in Fig. 13(a) and respectively by experimental results of Fig. 13(b) and Fig. 13(c). Again, the same experimental parameters of Case Study 5.5 are considered, with control window and transmission rate readjusted to occur once at each fundamental cycle (i.e., f_{CBC} = 16.66 ms). Such cases are respectively represented by two scenarios in Fig. 13(a), on which the first demonstrates the operation of the

CBC algorithm when EGs take different times to receive and process the control packets broadcasted by the CC (e.g., EGs with different distances from the CC, where EG_2 is farther than EG_1). The second scenario considers the unusual possibility of having even slower delays than expected at a given control cycle.

In Fig. 13(a) two EGs are sharing active, reactive, and harmonic currents, and the given control cycle $k = 1$ represents a new operational condition on the MG, which is emulated by the same load step of Fig. 8(f) and Fig. 8(g), demanding the CBC to adjust its coefficients. However, SPI_2 presents slower time (i.e., higher delay) to receive the control packets broadcasted by the CC. When a new control window begins (note the dashed pink bars in Fig. 13(a)), the CC saves a timestamp for that control cycle and communicates with the EGs to obtain the required actual current terms, which are then sent as demonstrated by the blue dashed bars. Now, SPI_1 takes approximately 1/4 of fundamental cycle to respond to the new scaling coefficients (i.e., delay D_1) and SPI_2 delays 3/4 (D_2) to receive the packet respective to control cycle $k = 2$ and to change its local current references. This process occurs repetitively, and as can be seen in the experiment of Fig. 13(b), upon receiving the broadcasted packets within the same control cycle, such delays D_1 and D_2 do not affect the overall ability of the CBC to steer EGs for current sharing, behaving similarly to the cases discussed in Fig. 8. It is remarked that such delays are emulated by counters that hold the control data packets by the desired time until released to EGs as seen in Fig. 7. It is also worth to remark that the results are shown here with a small time scale (i.e., some fundamental cycles) to simplify understanding. Of course, although in practical applications the communication between CC and EGs upon the beginning of a new control window should be considered larger, it could be simply seen as a time constant added to D_1 and D_2, not affecting the overall analysis herein discussed.

Regardless of the reasons, broadcasted data is likely to suffer with unusual delays, which may be greater than the expected (D_1 and/or D_2) for the operation of EGs while participating on CBC. Hence, Scenario 2 presents a case on which data packets of given control cycles delay excessively. Note in Fig. 13(a) that, when the CC gathers data to start cycle $k = 2$ and broadcast the respective control packet, SPI_1 still operates as in Scenario 1, with D_1 equal to 1/4 of fundamental period. Nonetheless, SPI_2's data packet for $k = 2$ delays excessively ($D_2^{'}$) and arrives only after a new control cycle started on $k = 3$. Since each control packet sent by the CC presents a header with a timestamp, also considering that all EGs know the actual control cycle by the previous communication established to send data to the CC, the packet related to $D_2^{'}$ cannot be used by SPI_2. Thus SPI_2 does not change its actual current references until a packet respective to the correct control cycle arrives. Observing cycles $k = 3$ and $k = 4$ one can note that, the control packet respective to $k = 3$ also delayed by $D_2^{''}$ and could not be used. Parallel to that, when $k = 4$ started, the communication issue on the broadcast for SPI_2 was solved, and another control packet arrived within this same control cycle with delay (D_2). Since the packet related to D_2 presents the right timestamp, it is the only one used, and SPI_2 then responds promptly as seen in Fig. 13(c). Note that data packet loss can be treated

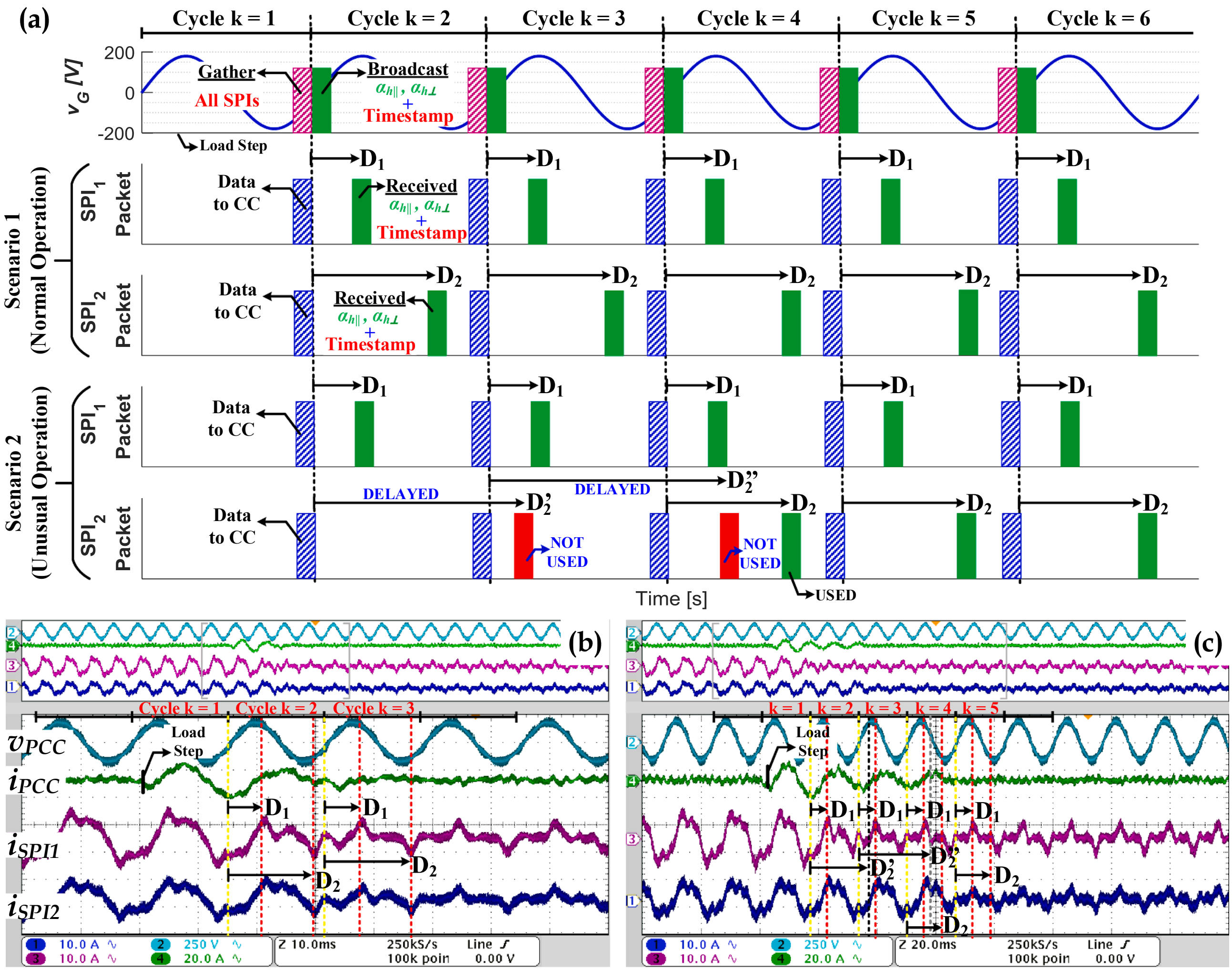

Fig. 13. Analysis of packet delays during the CBC operation. (a) Possible scenarios considering delayed control packets from the CC to SPIs. (b) Experimental result for Scenario 1. (c) Experimental result for Scenario 2.

likewise excessively delayed packets, not affecting the actual current references of SPIs until the right control cycle packet arrives.

All in all, this study case can be summarized by stating that even if packet delays occur, the CBC algorithm is robust to go through such inconsistencies, not affecting the local operation of primary controllers, neither jeopardizing system stability. In general, delays mostly affect the time response of SPIs upon changes occurring on the MG, as a consequence of the respective data transmission required for the processing of the CBC algorithm and re-calculation of scaling coefficients.

6. Conclusions

A centralized current-based control for distributed generators in low-voltage microgrids is discussed in this paper. The control is capable of accurately sharing among the distributed units the active, reactive, and harmonic current needs of the microgrid, without any knowledge of the network topology and parameters. The central controller receives as input only peak (magnitude) current terms and coordinates active, reactive, and harmonic current contributions from switching power interfaces to ensure a proportional power sharing; this allows distributed compensation of loads power needs, uniform exploitation of distributed inverters (e.g., in terms of thermal stresses), improved distribution efficiency and accurate adaptation to varying power demands from loads or the main grid. Communication requirements are low in terms of transmission rates and amount of exchanged information. Experimental and simulation results show that the proposed approach attains fully dispatchable power flow and high power factor at PCC, quick response to load steps, prompt reaction to grid voltage variations, plug-and-play capability, effective operation under limited converter capability and heavy voltage distortion, while performing the distributed selective harmonic compensation. Such control presents high robustness against parameters variations, and communication issues do not impair system stability, showing to be an appealing solution for advanced low-voltage microgrids.

Declaration of Competing Interest

The authors declare that they have no known competing financial interests or personal relationships that could have appeared to influence the work reported in this paper.

Acknowledgements

The authors are grateful to the Sao Paulo Research Foundation (FAPESP) (Grants 2018/22172-1, 2017/24652-8, 2016/08645-9), the Research Council of Norway (Grant f261735/H30), and the Brazilian government agencies CAPES and CNPq for their financial support.

References

[1] Arrillaga J, Watson NR. Effects on harmonic distortion. Power System Harmonics. WILEY. Chichester, UK: John Wiley & Sons, Ltd; 2003.

[2] Karuppanan P, Mahapatra KK. Active harmonic current compensation to enhance power quality. Int J Electr Power Energy Syst 2014;62:144–51.

[3] Rocabert J, Luna A, Blaabjerg F, Rodriguez P. Control of power converters in AC microgrids. IEEE Trans Power Electron 2012;27:4734–49.

[4] Akagi H. New tends in active filters for power conditioning. IEEE Trans Ind Appl 1996;32:1312–22.

[5] Guerrero JM, Chandokar M, Lee T, Loh PC. Advanced control architectures for intelligent microgrids—Part I: decentralized and hierarchical control. IEEE Trans Ind Electron 2012;60:1254–62.

[6] Antunes HMA, Silva SM, Brandao DI, Machado AAP, Filho BJC. A new multifunctional converter based on a series compensator applied to AC microgrids. Int J Electr Power Energy Syst 2018;102:160–70.

[7] Marafao FP, Brandao DI, Costabeber A, Paredes HKM. Multi-task control strategy for grid-tied inverters based on conservative power theory. IET Renew Power Gen 2015;9:154–65.

[8] Agundis-Tinajero G, Ramírez JS, Cruz NV, Savaghebi M, Guerrero JM, Barocio E. Power flow modeling of islanded AC microgrids with hierarchical control. Int J Electr Power Energy Syst 2019;105:28–36.

[9] Ziouani I, et al. Hierarchical control for flexible microgrid based on three-phase voltage source inverters operated in parallel. Int J Electr Power Energy Syst 2018;95(188):201.

[10] Han Y, et al. Review of active and reactive power sharing strategies in hierarchical controlled microgrids. IEEE Trans Power Electron 2017;32:2427–51.

[11] Han H, et al. Review of power sharing control strategies for islanding operation of AC microgrids. IEEE Trans Smart Grid 2016;7:200–2015.

[12] Yazdanian M, Sani A. Distributed control techniques in microgrids. IEEE Trans Smart Grid 2014;5:2901–9.

[13] Fani B, Zandi F, Karami-Horestani A. An enhanced decentralized reactive power sharing strategy for inverter-based microgrid. Int J Electr Power Energy Syst 2018;98:531–42.

[14] Mousavi SYM, Jalilian A, Savaghebi M, Guerrero JM. Autonomous control of current and voltage controlled DG interface inverters for reactive power sharing and harmonics compensation in islanded microgrids. IEEE Trans Power Electron 2018;33:9375–86.

[15] Golsorkhi MS, Lu DD, Guerrero JM. A GPS-based decentralized control method for islanded microgrids. IEEE Trans Power Electron 2017;32:1615–25.

[16] Li Y, Fan L. Stability analysis of two parallel converters with voltage-current droop control. IEEE Trans Power Del 2017;32:2389–97.

[17] Sreekumar P, Khadikar. A new virtual harmonic impedance scheme for harmonic power sharing in an Islanded microgrid. IEEE Trans Power Del 2016;31:936–45.

[18] Golsorkhi MS, Lu DD. A decentralized control method for islanded microgrids under unbalanced conditions. IEEE Trans Power Del 2016;31:1112–21.

[19] Micallef A, Apap M, Staines CS, Guerrero JM. Mitigation of harmonics in grid-connected and islanded microgrids via virtual admittances and impedances. IEEE Trans Smart Grid 2017;8:651–61.

[20] Hashempour MM, Savaghebi M, Vasquez JC, Guerrero JM. A control architecture to coordinate distributed generators and active power filters coexisting in a microgrid. IEEE Trans Smart Grid 2016;7:2325–36.

[21] Zhou J, et al. Consensus-based distributed control for accurate reactive, harmonic and imbalance power sharing in microgrids. IEEE Trans Smart Grid 2017;9:2453–67.

[22] Gao Y, Ai Q. Distributed cooperative optimal control architecture for AC microgrid with renewable generation and storage. Int J Electr Power Energy Syst 2018;96:324–34.

[23] Sreekumar P, Khadkikar V. Direct control of the inverter impedance to achieve controllable harmonic sharing in the islanded microgrid. IEEE Trans Ind Electron 2017;64:827–37.

[24] Lorzadeh I, Abyaneh HA, Savavhebi M, Guerrero JM. A hierarchical control scheme for reactive power and harmonic current sharing in islanded microgrids. Eur Conf Power Electron Appl 2015:1–10.

[25] Guan Y, et al. A novel harmonic current sharing control strategy for parallel-connected inverters. Energy Conv Cong Exp. IEEE; 2017.

[26] Caldognetto T, Buso S, Tenti P, Brandao DI. Power-based control of low-voltage microgrids. IEEE J Emerg Sel Topics Power Electron 2015;3:1056–66.

[27] Brandao DI, Tenti P, Caldognetto T, Buso S. Control of utility interfaces in low-voltage microgrids. Braz J Power Electronics (SOBRAEP) 2015;20:373–82.

[28] Kwon J, Yoon S, Choi S. Indirect current control for seamless transfer of three-phase utility interactive inverters. IEEE Trans Power Electron 2011;27:773–81.

[29] Buso S, Caldognetto T, Liu Q. Analysis and experimental characterization of a large-bandwidth triple-loop controller for grid-tied inverters. IEEE Trans Power Electron 2018;34:1936–49.

[30] Mohamed YAI, Radwan AA. Hierarchical control system for robust microgrid operation and seamless mode transfer in active distribution systems. IEEE Trans Smart Grid 2011;2(352):362.

[31] IEEE Standard for Interconnection and Interoperability of Distributed Energy Resources with Associated Electric Power Systems Interfaces. IEEE Standard 1547; 2018.

[32] Benchmark Systems for Network Integration of Renewable and Distributed Energy Resources. CIGRE Task Force C6.04 - Technical Note 575, 2014;1–119.

[33] Tenti P, Caldognetto T. On microgrid evolution to local area energy network (E-LAN). IEEE Trans Smart Grid 2019;10:1567–76.

[34] Guerrero JM, et al. Hierarchical control of droop-controlled AC and DC microgrids – a general approach toward standardization. IEEE Trans Ind Electron 2011;58:158–72.

[35] Mattavelli P. A closed-loop selective harmonic compensation for active filters. IEEE Trans Ind Appl 2001;58:158–72.

[36] Padua MS, Deckmann SM, Marafao FP. Frequency-adjustable positive sequence detector for power conditioning applications. Power Electron Spec Conf. IEEE; 2008. p. 1928–34.

[37] Xavier LS, et al. Adaptive current control strategy for harmonic compensation in single-phase solar inverters. Electr Power Syst Research 2017;142:84–95.

[38] Yi P, Wang X, Sun Z. Instantaneous harmonic decomposition technique for three-phase current based on multiple reference coordinates. IET Electr Power Appl 2018;12:547–56.

[39] Held G. Understanding data communications: from fundamentals to networking. third ed. Joh Wiley & Sons; 2000.

[40] SunSpec Technology Overview. SunSpec Alliance - Technical Note 12040, 2015;1–8.

[41] SunSpec Logging in SolarEdge Inverters. SolarEdge SunSpec Alliance - Technical Note, 2019;1–29.

[42] Angioni A, et al. Coordinated voltage control in distribution grids with LTE based communication infrastructure. IEEE 15th Int Conf Environ Electr Eng 2015:2090–5.

[43] Lee T, Cheng P, Akagi H, Fujita H. A dynamic tuning method for distributed active filter system. IEEE Trans Ind Appl 2008;44:612–23.

[44] Jintakosonwit P, Fujita H, Akagi H, Ogasawara S. Implementation and performance of cooperative control of shunt active filters for harmonic damping throughout a power distribution system. IEEE Trans Ind Appl 2003;39:556–64.
[45] Wada K, Fujita H, Akagi H. Considerations of a shunt active filter based on voltage detection for installation on a long distribution feeder. IEEE Trans Ind Appl 2002;38:1123–30.
[46] Ogata K. Discrete-time control systems. second ed. NJ: Prentice-Haal; 1994.
[47] Jayalath S, Hanif M. Generalized LCL-filter design algorithm for grid-connected voltage-source inverter. IEEE Trans Ind Electron 2017;64:1905–15.
[48] Buso S, Mattavelli P. Digital control in power electronics. second ed. Morgan& Claypool; 2015.
[49] Lu X, Guerrero JM, Sun K, Vasquez JC. An improved droop control method for DC microgrids based on low bandwidth communication with DC bus voltage restoration and enhanced current sharing accuracy. IEEE Trans Power Electron 2014;49:1800–12.
[50] Truong DQ, Ahn KK. Robust variable sampling period control for networked control systems. IEEE Trans Ind Electron 2015;69:5630–43.
[51] Zhang Y, Ma H. Theoretical and experimental investigation of networked control for parallel operation of inverters. IEEE Trans Ind Electron 2012;59:1961–71.
[52] Zhang Y. Analysis methodology for evaluation of time-delay impact on network-based system for droop-controlled AC microgrid. MDPI Electron 2019;8:1–23.